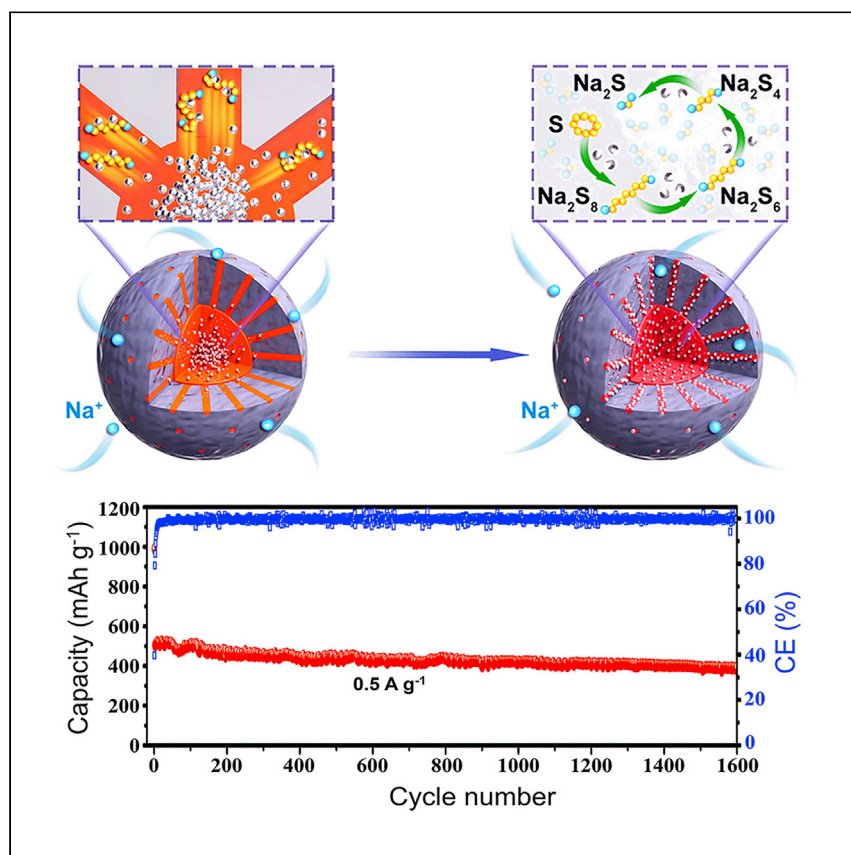


Article

Electrochemical release of catalysts in nanoreactors for solid sulfur redox reactions in room-temperature sodium-sulfur batteries



Mobile catalytic nanoparticles can overcome the constraints of stationary electrocatalytic sites for efficient polysulfide nucleation. Yan et al. visualize the electrochemical release of an ultrafine silver electrocatalyst to maximize electrocatalytic efficiency in nanoreactors. This work provides insights into the electrochemical self-releasing strategy for ultra-stable room-temperature Na/S batteries.

Zichao Yan, Qiang Tian, Yaru Liang, ..., -gnskip-->Gao-Qing (Max) Lu, Huakun Liu, Shi-Xue Dou

yunxiao@uow.edu.au (Y.-X.W.)
jian.liu@surrey.ac.uk (J.L.)
shulei@uow.edu.au (S.-L.C.)

Highlights

Visualization of dynamic electrochemical releasing catalysts

High electrocatalytic efficiency for nucleation of Na_2S

Facile construction of porous carbon-based nanoreactors

Ultra-stable room-temperature sodium-sulfur battery cathode

Yan et al., Cell Reports Physical Science 2, 100539
August 18, 2021 © 2021 The Author(s).
<https://doi.org/10.1016/j.xcrp.2021.100539>



Article

Electrochemical release of catalysts in nanoreactors for solid sulfur redox reactions in room-temperature sodium-sulfur batteries

Zichao Yan,^{1,2} Qiang Tian,³ Yaru Liang,² Lingyan Jing,³ Zhe Hu,⁶ Weibo Hua,⁴ Akhil Tayal,⁵ Weihong Lai,² Wanlin Wang,² Jian Peng,² Yun-Xiao Wang,^{2,*} Jian Liu,^{3,7,*} Shu-Lei Chou,^{2,6,8,*} Gao-Qing (Max) Lu,⁷ Huakun Liu,² and Shi-Xue Dou²

SUMMARY

Electrocatalysis-assisted entrapment of polysulfide while ensuring efficient nucleation of Na₂S holds the key to addressing the shuttle effect and sluggish kinetics of polysulfide in room-temperature (RT) Na/S batteries. The constrained active sites, however, dramatically limit the efficiency of electrocatalysts. Here, a strategy of electrochemically releasing nano-silver catalytic sites during the discharge process is presented, visualized, and implemented for accelerated Na₂S nucleation. Because of the effective polysulfide immobilization and accelerated Na₂S nucleation, the sulfur cathode, supported by a self-released silver electrocatalyst, exhibits a superior reversible capacity of 701 mAh g⁻¹ at 0.1 A g⁻¹ and an ultra-stable cycling performance. Precise understanding of the electrochemically self-releasing mechanism and the catalysis in Na₂S nucleation via *in situ* transmission electron microscopy (TEM) would aid, however, in fundamentally optimizing the working mechanism and for further development of more stable high-power RT Na/S batteries.

INTRODUCTION

Development of sulfur-based energy storage systems (ESS) with high theoretical capacity and eco-friendliness has attracted tremendous interest to meet increasing demands.^{1–4} Nevertheless, manufacturing ESSs on a massive scale based on conventional Li-ion storage is very expensive because of the scarcity and long-term consumption of Li resources.⁵ Therefore, a low-cost sulfur-based cathode in sodium ESS with superior capacity (1,675 mA h g⁻¹) and energy density (1,274 W h kg⁻¹) operated at room temperature has attracted tremendous interest for building inexpensive and efficient stationary ESSs.⁶ Similar to all alkali metal-S batteries, the poor performance of room-temperature (RT) Na/S batteries, which suffer from rapid capacity fading and low reversible capacity, is due to the sluggish kinetics of sulfur and its Na₂S product as well as the well-known polysulfide shuttling mechanism.⁷ To prevent undesirable active material transport and insufficient conversion of sulfur species caused by the sluggish kinetics and shuttle effect, research has been directed toward constructing porous carbon hosts, such as microporous carbon nanotubes,⁸ mesoporous hollow carbon nanospheres,^{9–13} hollow carbon spheres,¹⁴ nitrogen-doped porous carbon polyhedra,¹⁵ carbon fiber,¹⁶ etc. The nonpolar nature of carbon hosts with weak van der Waals interaction to polar polysulfides has further triggered interest in finding more suitable hosts. Importing polar components that offer strong chemical bonding with polysulfides, including several polar polymers, metal oxides, metal sulfides, MXene nanosheets, selenides, etc.,^{17–27} has

¹State Key Laboratory of Chemo/Biosensing and Chemometrics, College of Chemistry and Chemical Engineering, Hunan University, Changsha 410082, China

²Institute for Superconducting & Electronic Materials, Australian Institute of Innovative Materials, University of Wollongong, Innovation Campus, Squires Way, North Wollongong, NSW 2500, Australia

³State Key Laboratory of Catalysis, Dalian Institute of Chemical Physics, Chinese Academy of Sciences, Dalian 116023, China

⁴Institute for Applied Materials, Karlsruhe Institute of Technology, Eggenstein-Leopoldshafen 76344, Germany

⁵Deutsches Elektronen-Synchrotron (DESY), Hamburg 22607, Germany

⁶Institute for Carbon Neutralization, College of Chemistry and Materials Engineering, Wenzhou University, Wenzhou, Zhejiang 325035, China

⁷DICP-Surrey Joint Centre for Future Materials, Department of Chemical and Process Engineering, and Advanced Technology Institute, University of Surrey, Guilford, Surrey GU2 7XH, UK

⁸Lead contact

*Correspondence: yunxiao@uow.edu.au (Y.-X.W.), jian.liu@surrey.ac.uk (J.L.), shulei@uow.edu.au (S.-L.C.)

<https://doi.org/10.1016/j.xcrp.2021.100539>



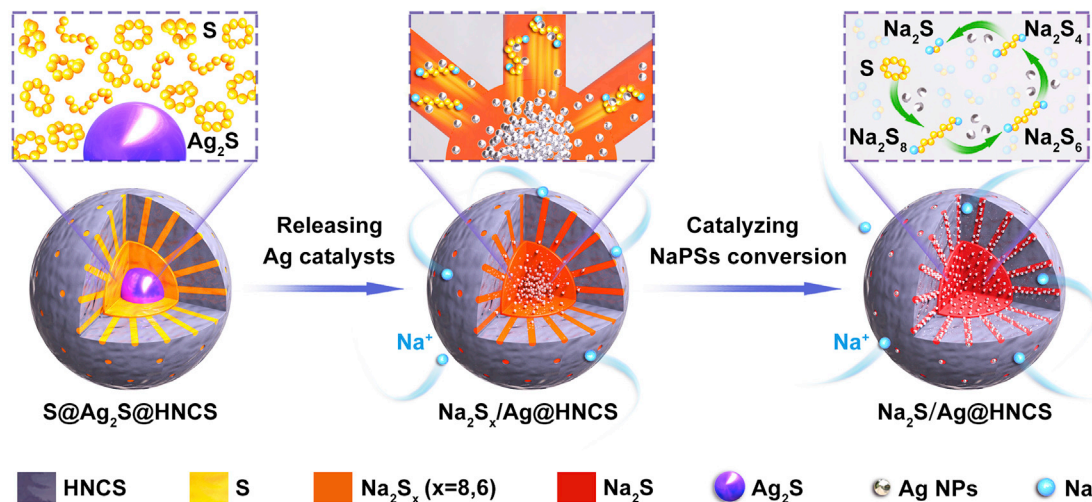


Figure 1. Schematic

The catalyst release process and the electrocatalytic mechanism of the yolk-shell cathode with Ag_2S and S encapsulated in hollow nitrogen-doped carbon spheres ($\text{S}@Ag_2\text{S}@HNCS$).

been investigated extensively. In contrast to the abovementioned approaches, embedding electrocatalysts in the carbon host to catalyze nucleation of Na_2S has been regarded as a new strategy for immobilizing polysulfides from a kinetics perspective.^{22,28,29} We recently reported that such an electrocatalyst can dramatically enhance the electrochemical performance of RT Na/S batteries, but the proposed mechanism of the polysulfide nucleation kinetics was hypothesized without visible evidence.²⁹ Because of the solid-state catalytic mechanism, the electrocatalytic efficiency toward poor activity and shuttle effects of sulfur species are highly influenced by the particle size of electrocatalysts and the direct contact area between electrocatalysts and S.^{28,30–34} Therefore, it is necessary to design a novel electrocatalyst for efficient solid S_8 redox reactions and evaluate its reliability.

To overcome the constraints of electrocatalytic sites for efficient polysulfide nucleation and visualize the electrocatalytic mechanism of the polysulfide nucleation kinetics, a novel strategy of electrochemically self-releasing electrocatalytic sites for efficient nucleation of Na_2S has been proposed. In this study, a large amount of bulk sulfur is encapsulated in the hollow space of a yolk-shell nanoreactor in which the motion process of Na_2S nucleation along with an *in situ* electrochemically released ultrafine Ag electrocatalyst can be visualized. The resultant active sites and highly directional spreading of Ag can maximize electrocatalytic efficiency by exposing abundant Ag ultrafine sites and offering effective contact for encapsulated S in the core and carbon shell. As shown in Figure 1, along with the S redox reactions during the sodiation process, numerous electrocatalytic Ag sites could be released dynamically and spread to the entire carbon skeleton through the inner porosity channels. Dispersion of the ultrafine Ag electrocatalyst, driven by the high affinity of the Ag-S interaction, achieves high electrocatalytic efficiency for nucleation of Na_2S , making the electrochemically self-releasing strategy a preferred choice for ultra-stable RT Na/S batteries.

RESULTS

Materials characterizations

A facile one-pot method to synthesize the yolk-shell nanoreactor containing silver cores is illustrated schematically in Figure 2A. Vesicles are formed to stabilize the

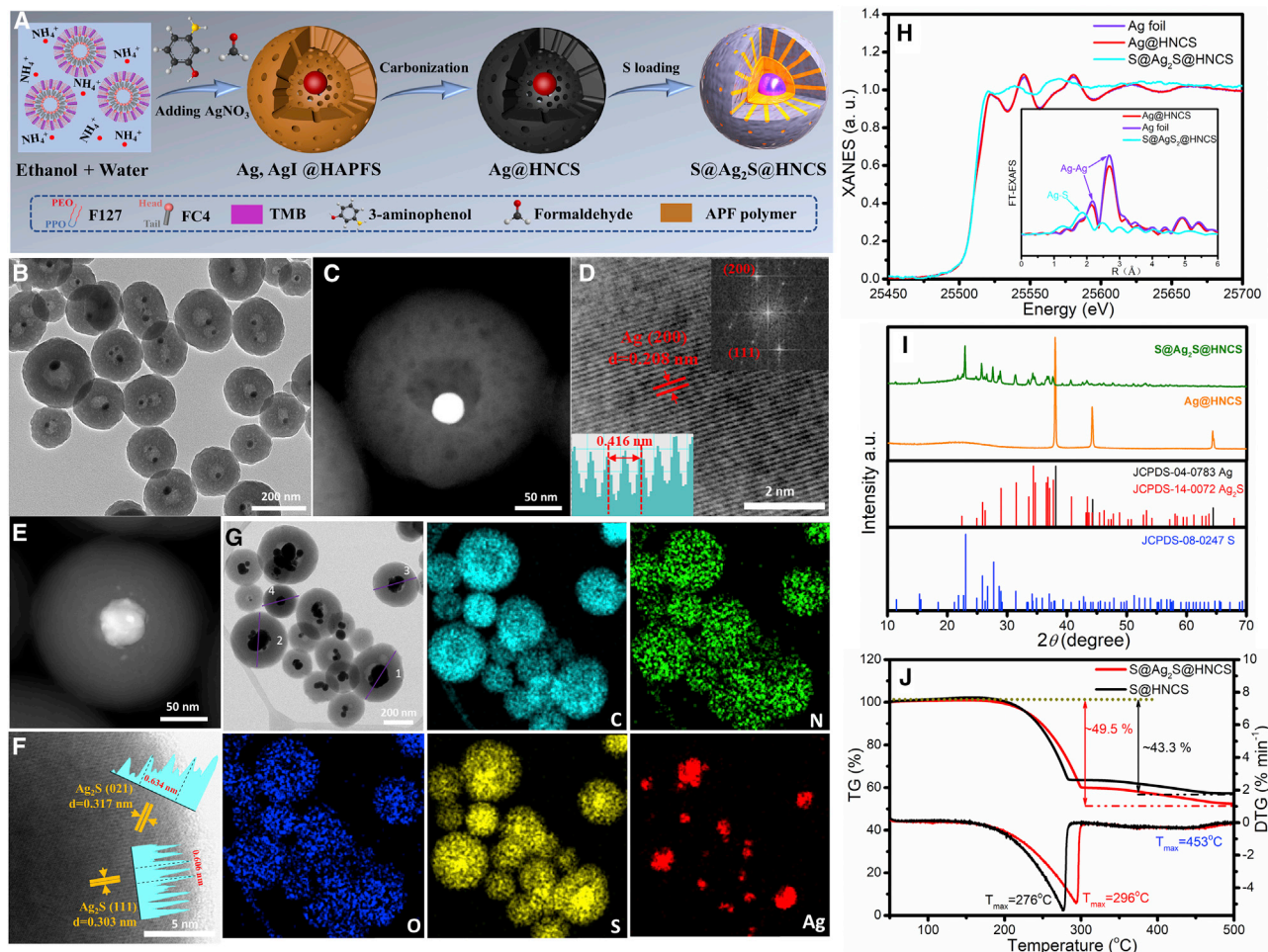


Figure 2. Synthesis, morphology, phase structure, XAS, and thermogravimetric analysis

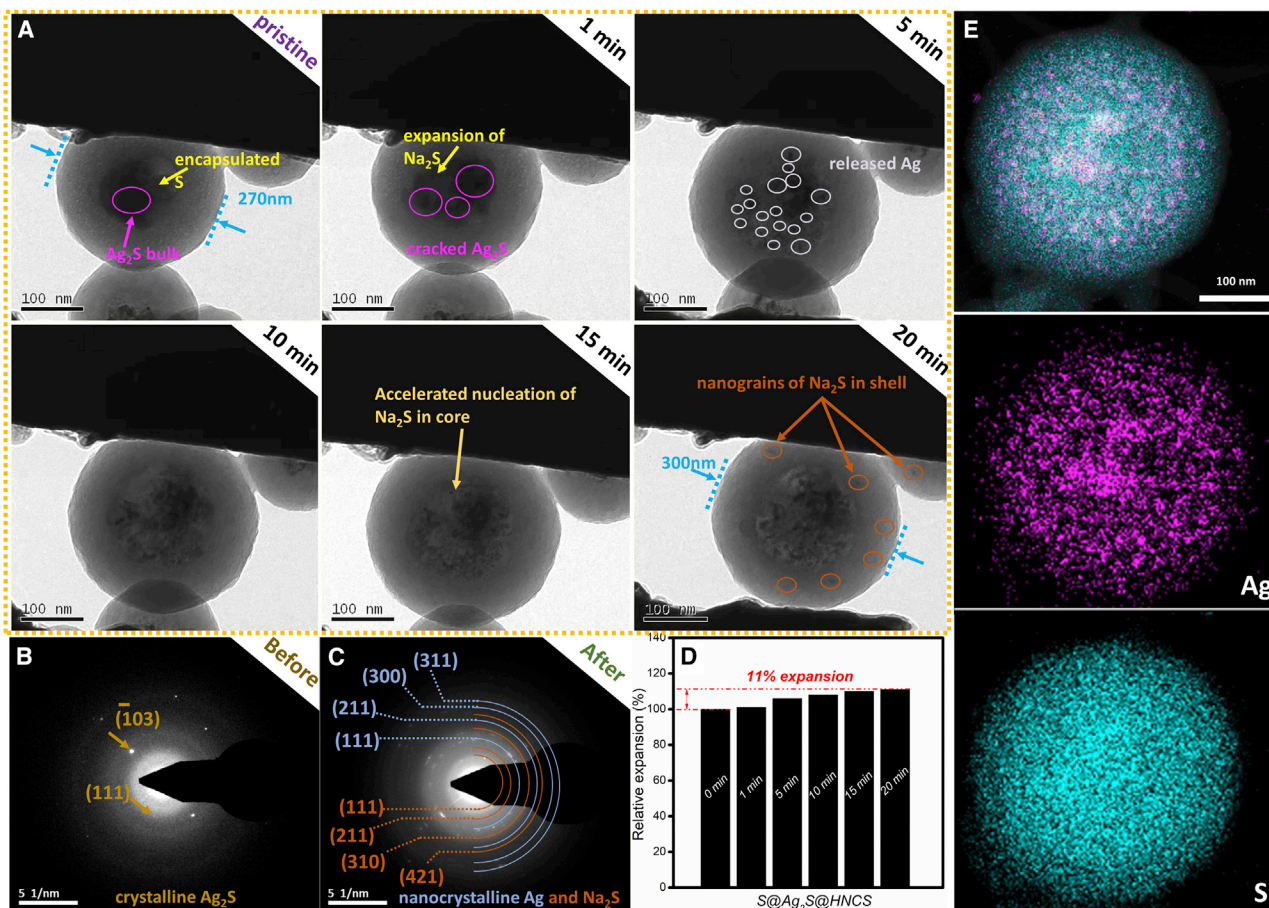
(A) Schematic of the synthetic process for the S@Ag₂S@HNCS cathode.
 (B) TEM image.
 (C and D) HAADF-STEM and HRTEM images with the corresponding FFT pattern (top right inset) of the Ag@HNCS.
 (E and F) HAADF-STEM and HRTEM images of S@Ag₂S@HNCS.
 (G) EDS mapping.
 (H) XANES with the corresponding FT-EXAFS spectra as inset.
 (I) XRD patterns of S@Ag₂S@HNCS and Ag@HNCS.
 (J) TGA of S@Ag₂S@HNCS and S@HNCS.

AgI-core nanoparticles by mixing the vesicle-manufacturing agent C₃F₇O (CFCF₃CF₂O)₂CFCF₃CONH(CH₂)₃N⁺(C₂H₅)₂CH₃⁺ (FC4; a fluorocarbon surfactant), the pore-forming agent F127 (PEO₁₀₆PPO₇₀PEO₁₀₆), and the pore-expanding agent TMB (1,3,5-trimethylbenzene) in a hydroalcoholic environment. By formaldehyde reducing Ag⁺ to Ag⁰ and forming aminophenol formaldehyde (APF) polymer, the yolk-shell structured precursor was obtained. After the carbonization and sulfur loading processes, the silver particles were fully oxidized to silver sulfide because of the superior affinity between Ag and sulfur (2Ag + S = Ag₂S, ΔH = −80 kJ mol^{−1}) (data collected from the Materials Project: <http://www.materialsproject.org>). The routine characterizations of the Ag@hollow nitrogen-doped carbon sphere (HNCS) precursor and its silver-free comparison sample are detailed in Figure S1. Transmission electron microscopy (TEM) images of Ag@HNCS (Figure 2B) with an overall Ag content of 16.5% (Figure S2) show homogeneously monodispersed

nanospheres with an average diameter of 200 nm. The yolk-shell nanoreactor with homogeneous element distribution exhibited uniform thickness of the shell and inner cavity to capture Ag particles (Figure S3). Numerous nanocavities emerged in the carbon shell with a diameter of ~ 5 nm, as revealed by high-angle annular dark-field (HAADF) images (Figure 2C), which strongly indicated its capability to physically entrap the polysulfides. A high-resolution TEM (HRTEM) image (Figure 2D) of an Ag particle reveals a measured interplanar distance of 0.208 nm, which represents the d -spacing of the (200) planes of Ag, and the corresponding fast Fourier transform (FFT) pattern contains the diffraction spots from the (111) and (200) planes of cubic Ag. After the sulfur loading process, the Ag is sulfurized into Ag_2S , and the scanning TEM (STEM) images of $\text{S@Ag}_2\text{S@HNCS}$ show less transparency compared with its Ag@HNCS precursor (Figure S3), indicating successful encapsulation of sulfur. An HAADF image (Figure 2E) of a monodispersed nanosphere shows that the inner cavity and the nanocavities of the amorphous carbon shell (Figure S4A) are occupied by elemental sulfur. The measured interplanar distances of 0.310 and 0.256 nm in core particle are well matched with the d -spacings of the corresponding (111) and (021) planes of Ag_2S (Figure 2F). The X-ray absorption near-edge structure (XANES) of the Ag K-edge in the sulfur-loaded composite provides a shifted absorption edge compared with standard Ag foil and the Ag@HNCS host, indicating the oxidation status of Ag atoms (Figure 2H). This is in agreement with the corresponding extended X-ray absorption fine structure (EXAFS) spectra, which showed distinctive Ag-S and Ag-Ag coordination in $\text{S@Ag}_2\text{S@HNCS}$ and Ag@HNCS respectively, firmly indicating sulfurization of Ag in the macroscopic view.³⁵ The energy dispersive spectroscopy (EDS) mapping images verify the homogeneous distribution of S along the carbon skeleton and cavities (Figure 2G). This is consistent with the composition analysis of $\text{S@Ag}_2\text{S@HNCS}$, where a small quantity of sulfur is observed on the surface by X-ray photoelectron spectroscopy (XPS), indicating that the majority of sulfur is encapsulated in inner cavities (Figures S4B and S4C). The elemental S and Ag_2S particles in the inner cavity are identified by sequential HAADF images of $\text{S@Ag}_2\text{S@HNCS}$ collected by unremitting beamline exposure (Figures S5 and S6; Video S1). The element S under the electron beamline became liquid and mobile first and finally sublimed within 20 s, whereas the immobile Ag_2S particles with intact sphere morphology could be fully retained.³⁶ This is in accordance with the EDS line scanning (Figure S7A) of individual particles. The X-ray diffraction (XRD) analysis in Figure 2I with strong peaks of sulfur confirms the domination of elemental sulfur in the cathode (Ag_2S can be observed in Figure S7B, the XRD pattern with sulfur removed), which is consistent with the thermogravimetric analysis (TGA). The sulfur content in the cathode was measured to be 49.5%, with the maximum weight loss rate (T_{max}) occurring at 296°C, which is 20°C higher than the S@HNCS composite. This is likely related to absorption of S on the Ag_2S surface. The slight weight loss at high temperature, with T_{max} of 453°C, can be attributed to the release of sulfur locked within the micropores; thus, a higher temperature is required to overcome the strong capillary force (Figure 2J).

Visible demonstration of catalyst release and its mechanism

To visually track the nucleation of Na_2S and demonstrate the dynamically self-releasing strategy of the Ag electrocatalysts, the sodiation process of the $\text{S@Ag}_2\text{S@HNCS}$ cathode was recorded using *in situ* TEM (Video S2). The Ag_2S spherical particles dynamically turned into ultrafine Ag nanoparticles with more exposed electrocatalytic sites during the sodiation process and are spread homogeneously along with expansion of sulfur species in the inner cavity (Figure 3A). The hollow space in the core of $\text{S@Ag}_2\text{S@HNCS}$ showed variable transparency during the sodiation process, indicating quasi-solid conversion of sulfur- Na_2S_x and



Na₂S_x-Na₂S. Interestingly, the polysulfides that are in direct contact with the ultrafine Ag electrocatalyst become less mobile. Finally, the anchored Na₂S nanograins are observed in the inner cavity, which can be attributed to the kinetically optimized nucleation of Na₂S by the highly efficient ultrafine electrocatalyst. In comparison, the nucleation process for sulfur species in carbon shells without the electrocatalyst is slower than that in the inner cavity. The calculated interfacial energy (γ) with respect to the number of Na₂S layers for the Ag/Na₂S and C/Na₂S interfaces is shown in Figure S8. The interfacial energy of the (220) Na₂S on the (200) Ag reaches a stable value of approximately -1.8 J/m^2 , which can be regarded to the minimal lattice mismatch.³⁷ Thus, it is easier to form more stable crystallinity of Na₂S on an Ag substrate. Experimentally, as shown in Figure S9, the solid sulfur reduction is studied by linear sweep voltammetry (LSV) and corresponding Tafel curves. The Ag-assisted cathode with higher catalytic activity for solid sulfur reduction reduces the overpotential by $\sim 15 \text{ mV}$ (0.08 mA cm^{-2}) from the 6th to the 25th cycle and the Tafel slope from 300 mV dec^{-1} to 286 mV dec^{-1} . In comparison, the Ag-free cathode shows much higher values for overpotential and Tafel slope, indicating poor conversion kinetics of solid sulfur.³⁸ Therefore, the released Ag electrocatalyst can not only provide a stable interface for Na₂S nucleation but also catalyze conversion of the solid

sulfur cathode. As shown in their corresponding selected area electron diffraction (SAED) patterns before and after the sodiation process (Figures 3B and 3C), the diffraction pattern of Ag_2S is observed in the pristine particle, and, finally, the polycrystalline structures of the ultrafine Ag and Na_2S nanograins are revealed with a slight volume expansion of 11% (Figure 3D), indicating successful conversion of S- Na_2S and Ag_2S -Ag, respectively. This was also confirmed by *ex situ* XRD patterns and HRTEM images (Figure S10) of the $\text{S@Ag}_2\text{S@HNCS}$ cathode in the sodiated state, where the broad peaks located at 38.0° and 38.8° can be attributed to the (111) and (220) planes of Ag and Na_2S nanograins, respectively. After 200 cycles, the Ag nanograins are dispersed homogeneously in the entire yolk-shell skeleton (Figure 3E), indicating that the dynamically obtained ultrafine Ag nanoparticles could further diffuse into the carbon shell through the interconnected cavities. In comparison, there is no sign of self-release or directional diffusion of Ag nanoparticles in the host for the sodiated $\text{Ag}_2\text{S@HNCS}$ electrode (Figure S11). The above results imply that the driving force for homogeneously diffusing and directionally moving ultrafine Ag nanoparticles in the $\text{S@Ag}_2\text{S@HNCS}$ could be attributed to continuous affinity between newly exposed silver and sulfur species rather than the phenomenon of Ag_2S conversion.

Electrochemical properties

Benefitting from the dynamically self-releasing electrocatalyst and the porous nano-reactors (Figure S12) in effectively confining polysulfides and catalyzing their conversion, the cathode delivered a highly reversible capacity of 701 mAh g^{-1} at 0.1 A g^{-1} and maintained it at 530 mAh g^{-1} for 200 cycles (Figure 4A). In comparison, the S@HNCS showed an extremely low Coulombic efficiency for the first cycle (28%) and dramatic capacity loss over 200 cycles, indicating incomplete conversion and shuttling of sulfur species. The corresponding charge/discharge plateaus of $\text{S@Ag}_2\text{S@HNCS}$ in Figure 4B shows two highly repeatable plateaus around 1.6 V and 0.9 V from the second cycle, indicating the reversible conversion reactions of the sulfur species with support of the dynamic electrocatalyst.^{21,39} The electrocatalyst-free electrode shows steep plateaus around 1.6 V and a relatively larger polarization value of 461 mV at the 10th cycle, and the value even increased to 650 mV for 200 cycles (Figure 4C). The improved reversible capacity and reductive polarization indicate that the released electrocatalytic sites can achieve high electrocatalytic efficiency for ultra-stable performance. This phenomenon is also reflecting on cyclic voltammograms (CVs) (Figures 4D and 4E). The prominent reduction peak around 2.0 V reflects the conversion of elemental sulfur in the first cathodic scan and disappeared from the second scan, which could be ascribed to the irreversible reduction between surface S_8 and carbonate solvents.⁹ This peak could still be detected in the following three cathodic scans for the S@HNCS cathode with dramatic current attenuation, indicating incomplete reduction of sulfur. This is also in good agreement with the low Coulombic efficiency of the initial cycle of S@HNCS and $\text{S@Ag}_2\text{S@HNCS}$, for which the irreversible side reactions, reduction of surface S_8 , and slow activation of active sites should be responsible. The other two repeatable cathodic peaks at 1.23 V and 0.92 V for $\text{S@Ag}_2\text{S@HNCS}$ respond to the reversible mechanism for formation of Na_2S_4 and Na_2S , respectively.²³ The S@HNCS cathode shows a single cathodic peak at 0.91 V, which can be ascribed to the sluggish kinetics of nucleation of the soluble Na_2S_x ($4 < x \leq 8$) to Na_2S , leading to a low reversible capacity and poor cycle life. Based on the abovementioned benefits, the $\text{S@Ag}_2\text{S@HNCS}$ cathode delivered ultra-stable performance, with a capacity of 391 mAh g^{-1} retained for 1,600 cycles at 0.5 A g^{-1} and improved rate performance by delivering 699, 605, 507, 399, and 275 mAh g^{-1} at current densities of 0.1, 0.2, 0.5, 1, and 2 A g^{-1} , respectively (Figures 4F and 4G). The unsatisfactory performance under 2 A g^{-1} could be

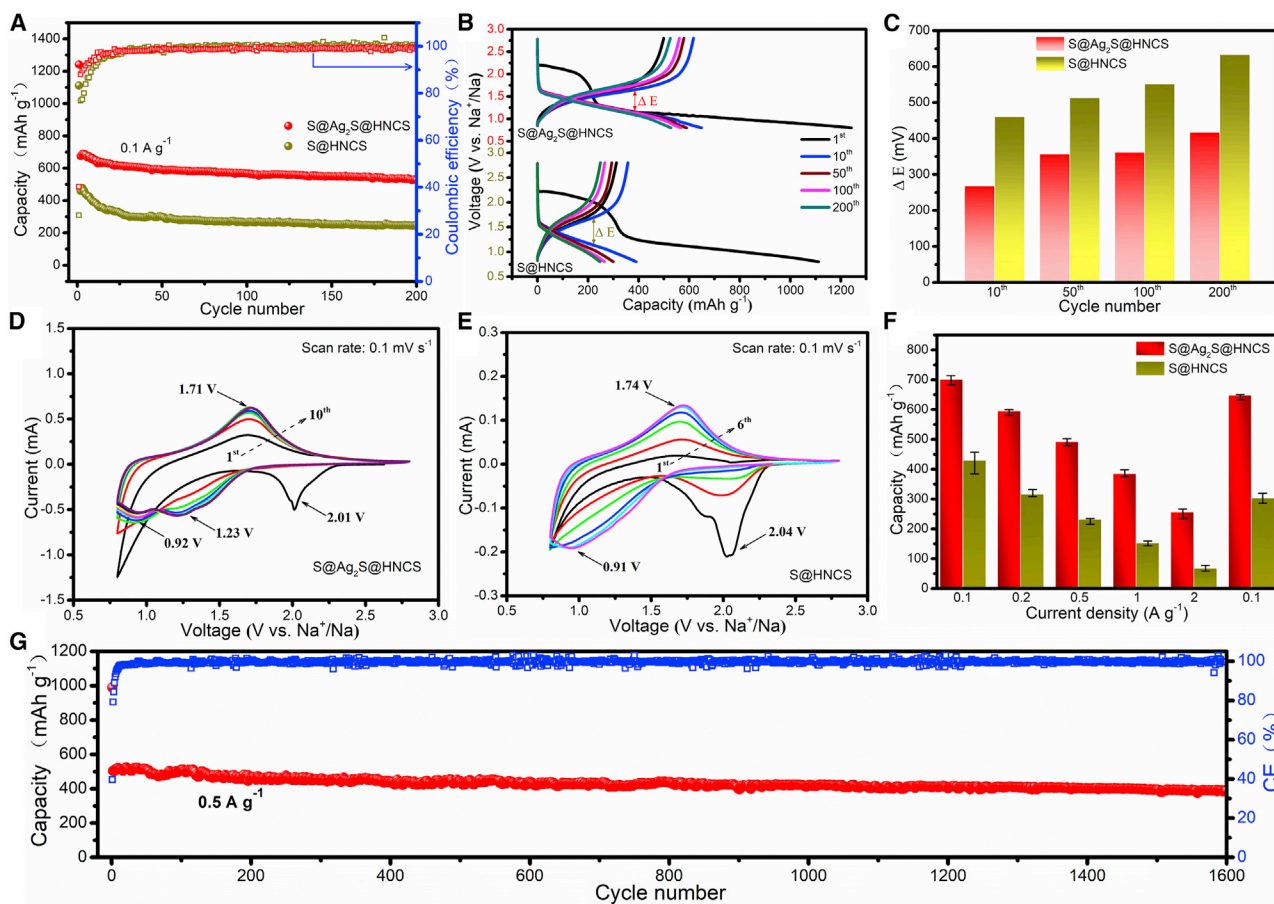


Figure 4. RT sodium-sulfur battery test

(A–F) Cycling performances (A), charge/discharge curves (B), polarization value in different cycles (C), cyclic voltammograms (CVs; D and E), and rate performance with capacity error bars of S@Ag₂S@HNCS and S@HNCS (F). The error bars represent the variation in the specific capacity of the batteries used during the rate test.

(G) Long-term cycling of S@Ag₂S@HNCS.

attributed to the poor conductivity of the solid S₈ cathode encapsulated in the core. Upon reverting back to a low rate, it showed 96% restored capacity, which is much higher than S@HNCS (62%). Besides, the charge/discharge curves of the S@Ag₂S@HNCS electrode are not as sloping as for the Ag free electrode, especially at high rates (Figure S13), indicating good electrocatalysis of the Ag nanoparticles.

DISCUSSION

We presented an electrochemical self-release strategy to achieve ultrafine catalysts and maximize their electrocatalytic efficiency for S redox reactions, which is realized by dynamically delivering ultrafine Ag sites into the entire nanoreactor through electrochemical conversion of Ag₂S yolks. The self-releasing process and optimized nucleation kinetics of Na₂S are visually tracked and confirmed by *in situ* TEM and density functional theory (DFT) calculation. The homogeneously dispersed Ag active sites can immobilize the polysulfides, achieving reversible conversion of Na₂S for encapsulated S in the core and carbon shell. The dynamic electrocatalyst-supported cathode achieved a 34% improvement in capacity retention after high-rate cycling and 41% enhancement in specific capacity. The electrochemical self-release strategy can dynamically optimize

the high affinity for hosting sulfur species in RT Na/S batteries, which gives new insights into improving the electrocatalytic efficiency of electrocatalysts.

EXPERIMENTAL PROCEDURES

Resource availability

Lead contact

Further information and requests for resources and reagents should be directed to and will be fulfilled by the lead contact, Shu-Lei Chou (shulei@uow.edu.au).

Materials availability

Materials used in this study will be made available upon request.

Data and code availability

Any additional information required to reanalyze the data reported in this article is available from the lead contact upon request.

Materials

Triblock poly(ethylene oxide)-b-poly(propylene oxide)-b-poly(ethylene oxide) pluronic F127 (Mw = 12,600) was purchased from Sigma-Aldrich. FC4 was purchased from Shanghai Intechem. 3-aminophenol (C₆H₇NO), ammonium hydroxide (NH₄OH, 28–30 wt %), formaldehyde solution (CH₂O, 37 wt %), TMB (C₉H₁₂), and ethanol (C₂H₆O) were purchased from Shanghai Chemical. All chemicals were of analytical grade and used without further purification. Deionized water was used for all experiments.

Synthesis of Ag, AgI@HAPFS, and HAPFS

In a typical synthesis, FC4 (0.16 g) and F127 (0.32 g) were dissolved in a mixture of water (20 mL) and ethanol (20 mL). Then 0.4 mL of TMB and 1.0 mL of ammonia were added to the reaction mixture under stirring at RT. When the mixture became milky white, an aqueous solution of silver nitrate (1.0 mL, 0.15 M) was added. After stirring at RT for 1 h, 3-aminophenol (0.2 g) and formaldehyde (0.28 mL) were added. The mixture was stirred for 24 h and subsequently heated for 24 h at 100°C under static conditions in a Teflon-lined autoclave. The Ag and AgI@HAPFS were recovered by centrifugation and air-dried at 60°C for 24 h. No silver nitrate was added in the synthesis of hollow aminophenol formaldehyde spheres (HAPFS).

Synthesis of Ag@HNCS and HNCS

To prepare corresponding carbide products, the obtained Ag, AgI@APFS, and HAPFS were heated at 2°C min⁻¹ from room temperature to 350°C and kept at this temperature for 2 h under a nitrogen atmosphere. The temperature was then further raised at 2°C min⁻¹ to 800°C and maintained for 6 h.

Synthesis of S@Ag₂S@HNCS and S@HNCS

To prepare corresponding vulcanization products, the obtained Ag@HNCS and HNCS were ground with sulfur in an agate mortar and sealed in a quartz tube and calcined at 155°C for 24 h and then at 300°C for 1 h to obtain the final S@Ag₂S@HNCS composite. For comparison, the S@HNCS was obtained under the same conditions.

Physical characterization

XRD patterns were employed with Cu K α radiation in the 2 θ range of 10°–70° (PANalytical diffractometer, λ = 1.5406 Å, step size of 0.02° s⁻¹). The morphology was detected via a field emission scanning electron microscope (FESEM; JEOL JSM-7500FA). A 200-kV scanning transmission electron microscope (JEM-ARM

200F) was equipped with a double aberration corrector to achieve SAED with a probe-forming, image-forming lens systems. The angular range of collected electrons for the HAADF images was around 70–250 mrad, and annular bright field (ABF)-STEM images were recorded simultaneously using a ABF detector. The EDS mapping results were obtained via STEM using Noran system SIX (NSS). *In situ* nanofabrication was carried out inside a transmission electron microscope (FEIT Tecnai F20st) using a TEM-STM (scanning tunnelling microscope) holder (Pico Femto FE02-ST) from Zeptools. XPS with Al K α radiation ($h\nu = 1,486.6$ eV) was employed to detect the binding energies using a SPECSPHOIBOS 100 analyzer installed in a chamber in a high vacuum. The porosity was measured by nitrogen sorption isotherms at 77 K with a Micromeritics Tristar 3020 analyzer (USA). Raman spectra were collected using a 10-mW helium/neon laser at 632.8-nm excitation, which was filtered by a neutral density filter to reduce the laser intensity, and a charge-coupled device (CCD). The thermal decomposition behavior of the products was monitored using a Mettler Toledo TGA/SDTA851 analyzer from 50°C to 500°C in Ar with a heating rate of 5°C/min. X-ray absorption spectroscopy (XAS) measurements were performed at the XAS beamline of the synchrotron radiation source at Deutsches Elektronen-Synchrotron (DESY). The XAS data were recorded at the Ag K-edge in transmission mode.

Electrochemical measurements

The working electrodes for sodium-sulfur cells with an average mass loading of 2.3 mg on punched circular working electrodes with an area of 0.7 cm^{−2} were fabricated by mixing the as-synthesized samples, carbon black, and carboxymethyl cellulose (CMC) binder at a weight ratio of 70:20:10 in water, which were then pasted on aluminum foil followed by drying under a vacuum at 55°C overnight. The test cells were assembled with metallic sodium as the negative electrode, a glass fiber separator (Whatman GF/F), and 1 M NaClO₄ in 1:1 ethylene carbonate (EC) /propylene carbonate (PC) and 3 wt % fluoroethylene carbonate (FEC) additive electrolyte. Assembly of the test cells was carried out in an argon-filled glovebox, where water and oxygen concentrations were kept at less than 0.1 ppm. The electrochemical properties were examined by a NEWARE test system with a cutoff voltage range of 0.8–2.8 V (versus Na/Na⁺). CV and impedance testing were performed using a Biologic VMP-3 electrochemical workstation from 0.8–2.8 V at a sweep rate of 0.1 mV s^{−1}. All batteries were rested overnight before testing.

Computational methods

First-principle calculations were conducted using DFT with the Vienna *Ab Initio* Simulation Package (VASP).^{40,41} The projector augmented wave (PAW) method was applied, and a cutoff energy of 500 eV was used. Generalized gradient approximation (GGA) with the Perdew-Burke-Ernzerhof (PBE) function was used to approximate exchange-correlation potential. The interfacial configurations were modeled based on Na₂S (220) and Ag (100). Gamma-centered K points were set to 5 × 4 × 1 for the Na₂S/Ag configuration and 5 × 8 × 1 for the Na₂S/C configuration. Atomic positions and cell vectors were fully optimized until all force components were less than 0.02 eV Å^{−1}. A vacuum layer of 15 Å was set to ensure no influence between slabs. The interfacial formation energy (γ) was calculated according to the following equations:

$$\gamma = \frac{E_{\text{Na}_2\text{S}/\text{PS}} - E_{\text{Na}_2\text{S}} - E_{\text{PS}}}{A} - \sigma_{\text{PS}} - \sigma_{\text{Na}_2\text{S}} \quad (\text{Equation 1})$$

$$\sigma_x = \frac{E_x - E_x^{\text{Bulk}}}{2A}, \quad (\text{Equation 2})$$

where PS represents the polar surface (C or Ag), $E_{Na_2S/PS}$ is the total energy of the Na_2S and polar surface after absorption, and σ_x and E_x^{Bulk} are defined as the surface energy and total energy of the corresponding total energy of Na_2S and PS in the bulk state.

SUPPLEMENTAL INFORMATION

Supplemental information can be found online at <https://doi.org/10.1016/j.xcrp.2021.100539>.

ACKNOWLEDGMENTS

The authors are grateful for financial support from an Australian Renewable Energy Agency (ARENA) project (G00849), the National Natural Science Foundation of China (21872159), the DNL Cooperation Fund, CAS (DNL180402), the Fundamental Research Funds for the Central Universities (531118010633), and the Australian Research Council (ARC) (DE170100928). The authors would like to thank Dr. Tania Silver for critical reading of the paper.

AUTHOR CONTRIBUTIONS

Z.Y., Q.T., and Y.L. contributed equally to this work. Z.Y., Q.T., and Y.L. performed synthesis and characterization and wrote the manuscript. Y.-X.W., J.L., and S.-L.C. supervised the project. W.H. and A.T. performed X-ray absorption spectroscopy. Z.H. performed the DFT calculations. Q.T. and L.J. conducted the precursor. W.L., W.W., and J.P. helped analyze the electrochemical data. Y.-X.W., J.L., S.-L.C., H.L., S.-X.D., and G.-Q.L. helped draft the manuscript.

DECLARATION OF INTERESTS

S.-L.C. is an advisory board member at *Cell Reports Physical Science*.

Received: June 9, 2021

Revised: July 6, 2021

Accepted: July 22, 2021

Published: August 11, 2021

REFERENCES

- Xue, W.J., Shi, Z., Suo, L.M., Wang, C., Wang, Z.A., Wang, H.Z., So, K.P., Maurano, A., Yu, D.W., Chen, Y.M., et al. (2019). Intercalation-conversion hybrid cathodes enabling Li-S full-cell architectures with jointly superior gravimetric and volumetric energy densities. *Nat. Energy* 4, 374–382.
- Chu, S., and Majumdar, A. (2012). Opportunities and challenges for a sustainable energy future. *Nature* 488, 294–303.
- Conder, J., Bouchet, R., Trabesinger, S., Marino, C., Gubler, L., and Villeveuille, C. (2017). Direct observation of lithium polysulfides in lithium-sulfur batteries using operando X-ray diffraction. *Nat. Energy* 2, 7.
- Wu, C., Zhu, Y., Guan, C., Jia, C.K., Qin, W., Wang, X.Y., and Zhang, K.L. (2019). Mesoporous aluminium manganese cobalt oxide with pentahedron structures for energy storage devices. *J. Mater. Chem. A Mater. Energy Sustain.* 7, 18417–18427.
- Yabuuchi, N., Kajiyama, M., Iwatate, J., Nishikawa, H., Hitomi, S., Okuyama, R., Usui, R., Yamada, Y., and Komaba, S. (2012). P2-type $Na_x[Fe_{(1/2)}Mn_{(1/2)}]O_2$ made from earth-abundant elements for rechargeable Na batteries. *Nat. Mater.* 11, 512–517.
- Wei, S., Xu, S., Agrawal, A., Choudhury, S., Lu, Y., Tu, Z., Ma, L., and Archer, L.A. (2016). A stable room-temperature sodium-sulfur battery. *Nat. Commun.* 7, 11722.
- Wang, Y.X., Zhang, B.W., Lai, W.H., Xu, Y.F., Chou, S.L., Liu, H.K., and Dou, S.X. (2017). Room-Temperature Sodium-Sulfur Batteries: A Comprehensive Review on Research Progress and Cell Chemistry. *Adv. Energy Mater.* 7, 17.
- Xin, S., Yin, Y.X., Guo, Y.G., and Wan, L.J. (2014). A high-energy room-temperature sodium-sulfur battery. *Adv. Mater.* 26, 1261–1265.
- Wang, Y.X., Yang, J., Lai, W., Chou, S.L., Gu, Q.F., Liu, H.K., Zhao, D., and Dou, S.X. (2016). Achieving High-Performance Room-Temperature Sodium-Sulfur Batteries With S@Interconnected Mesoporous Carbon Hollow Nanospheres. *J. Am. Chem. Soc.* 138, 16576–16579.
- Liu, Jian, Wickramaratne, Nilantha P., Qiao, Shizhang, and Jaroniec, Mietek (2015). Molecular-based Design and Emerging Applications of Nanoporous Carbon Spheres. *Nature Materials* 14 (76), 763–774.
- Tian, Hao, Liang, Ji, and Liu, Jian (2019). Nanoengineering Carbon Spheres as Nanoreactors for Sustainable Energy Applications. *Advanced Materials* 31, 1903886.
- Tian, Hao, Tian, Huajun, Wang, Shijian, Chen, Shuangming, Zhang, Fan, Song, Li, et al. (2020). High-power Lithium-selenium Batteries Enabled by Atomic Cobalt Electrocatalyst Incorporated in Hollow Carbon Cathode. *Nature Communications* 11, 5025.
- Boyjoo, Yash, Shi, Haodong, Tian, Qiang, Liu, Shaomin, Liang, Ji, Wu, Zhong-Shuai, et al. (2021). Energy Environmental Science 14, 540–575.

14. Lee, D.J., Park, J.W., Hasa, I., Sun, Y.K., Scrosati, B., and Hassoun, J. (2013). Alternative materials for sodium ion-sulphur batteries. *J. Mater. Chem. A Mater. Energy Sustain.* *1*, 5256–5261.
15. Yang, T.T., Gao, W., Guo, B.S., Zhan, R.M., Xu, Q.J., He, H., Bao, S.J., Li, X.Y., Chen, Y.M., and Xu, M.W. (2019). A railway-like network electrode design for room temperature Na-S rechargeable batteries operating at room temperature. *J. Mater. Chem. A Mater. Energy Sustain.* *7*, 150–156.
16. Hwang, T.H., Jung, D.S., Kim, J.S., Kim, B.G., and Choi, J.W. (2013). One-dimensional carbon-sulfur composite fibers for Na-S rechargeable batteries operating at room temperature. *Nano Lett.* *13*, 4532–4538.
17. Ma, D.T., Li, Y.L., Yang, J.B., Mi, H.W., Luo, S., Deng, L.B., Yan, C.Y., Rauf, M., Zhang, P.X., Sun, X.L., et al. (2018). New Strategy for Polysulfide Protection Based on Atomic Layer Deposition of TiO₂ onto Ferroelectric-Encapsulated Cathode: Toward Ultrastable Free-Standing Room Temperature Sodium-Sulfur Batteries. *Adv. Funct. Mater.* *28*, 9.
18. Yang, T., Guo, B., Du, W., Aslam, M.K., Tao, M., Zhong, W., Chen, Y., Bao, S.J., Zhang, X., and Xu, M. (2019). Design and Construction of Sodium Polysulfides Defense System for Room-Temperature Na-S Battery. *Adv. Sci. (Weinh.)* *6*, 1901557.
19. Wang, J.L., Yang, J., Nuli, Y., and Holze, R. (2007). Room temperature Na/S batteries with sulfur composite cathode materials. *Electrochem. Commun.* *9*, 31–34.
20. Zeng, L.C., Yao, Y., Shi, J.N., Jiang, Y., Li, W.H., Gu, L., and Yu, Y. (2016). A flexible S_{1-x}Se_x@porous carbon nanofibers (x≤0.1) thin film with high performance for Li-S batteries and room-temperature Na-S batteries. *Energy Storage Mater.* *5*, 50–57.
21. Wang, L.H., Chen, X., Li, S.P., Yang, J.Q., Sun, Y.L., Peng, L.F., Shan, B., and Xie, J. (2019). Effect of eutectic accelerator in selenium-doped sulfurized polyacrylonitrile for high performance room temperature sodium-sulfur batteries. *J. Mater. Chem. A Mater. Energy Sustain.* *7*, 12732–12739.
22. Yan, Z., Xiao, J., Lai, W., Wang, L., Gebert, F., Wang, Y., Gu, Q., Liu, H., Chou, S.L., Liu, H., and Dou, S.X. (2019). Nickel sulfide nanocrystals on nitrogen-doped porous carbon nanotubes with high-efficiency electrocatalysis for room-temperature sodium-sulfur batteries. *Nat. Commun.* *10*, 4793.
23. Bao, W., Shuck, C.E., Zhang, W., Guo, X., Gogotsi, Y., and Wang, G. (2019). Boosting Performance of Na-S Batteries Using Sulfur-Doped Ti₃C₂T_x MXene Nanosheets with a Strong Affinity to Sodium Polysulfides. *ACS Nano* *13*, 11500–11509.
24. Li, Z., Zhang, J., Lu, Y., and Lou, X.W.D. (2018). A pyrolyzed polyacrylonitrile/selenium disulfide composite cathode with remarkable lithium and sodium storage performances. *Sci. Adv.* *4*, eaat1687.
25. Zhang, J., Li, Z., Chen, Y., Gao, S., and Lou, X.W.D. (2018). Nickel-Iron Layered Double Hydroxide Hollow Polyhedrons as a Superior Sulfur Host for Lithium-Sulfur Batteries. *Angew. Chem. Int. Ed. Engl.* *57*, 10944–10948.
26. Sun, T.T., Zhao, X.M., Li, B., Shu, H.B., Luo, L.P., Xia, W.L., Chen, M.F., Zeng, P., Yang, X.K., Gao, P., et al. (2021). NiMoO₄ Nanosheets Anchored on N-S Doped Carbon Clothes with Hierarchical Structure as a Bidirectional Catalyst toward Accelerating Polysulfides Conversion for Li-S Battery. *Adv. Funct. Mater.* *31*, 11.
27. Liu, H., Lai, W.-H., Yang, Q., Lei, Y., Wu, C., Wang, N., Wang, Y.-X., Chou, S.-L., Liu, H.K., and Dou, S.X. (2021). Understanding Sulfur Redox Mechanisms in Different Electrolytes for Room-Temperature Na-S Batteries. *Nano-Micro Lett.* *13*, 121.
28. Al Salem, H., Babu, G., Rao, C.V., and Arava, L.M.R. (2015). Electrocatalytic Polysulfide Traps for Controlling Redox Shuttle Process of Li-S Batteries. *J. Am. Chem. Soc.* *137*, 11542–11545.
29. Zhang, B.W., Sheng, T., Liu, Y.D., Wang, Y.X., Zhang, L., Lai, W.H., Wang, L., Yang, J., Gu, Q.F., Chou, S.L., et al. (2018). Atomic cobalt as an efficient electrocatalyst in sulfur cathodes for superior room-temperature sodium-sulfur batteries. *Nat. Commun.* *9*, 4082.
30. Song, J., Gordin, M.L., Xu, T., Chen, S., Yu, Z., Sohn, H., Lu, J., Ren, Y., Duan, Y., and Wang, D. (2015). Strong lithium polysulfide chemisorption on electroactive sites of nitrogen-doped carbon composites for high-performance lithium-sulfur battery cathodes. *Angew. Chem. Int. Ed. Engl.* *54*, 4325–4329.
31. Du, L., Cheng, X., Gao, F., Li, Y., Bu, Y., Zhang, Z., Wu, Q., Yang, L., Wang, X., and Hu, Z. (2019). Electrocatalysis of S-doped carbon with weak polysulfide adsorption enhances lithium-sulfur battery performance. *Chem. Commun. (Camb.)* *55*, 6365–6368.
32. Ye, Z.Q., Jiang, Y., Feng, T., Wang, Z.H., Li, L., Wu, F., and Chen, R.J. (2020). Curbing polysulfide shuttling by synergistic engineering layer composed of supported Sn₄P₃ nanodots electrocatalyst in lithium-sulfur batteries. *Nano Energy* *70*, 9.
33. Lin, H.B., Yang, L.Q., Jiang, X., Li, G.C., Zhang, T.R., Yao, Q.F., Zheng, G.W., and Lee, J.Y. (2017). Electrocatalysis of polysulfide conversion by sulfur-deficient MoS₂ nanoflakes for lithium-sulfur batteries. *Energy Environ. Sci.* *10*, 1476–1486.
34. He, J.R., and Manthiram, A. (2019). A review on the status and challenges of electrocatalysts in lithium-sulfur batteries. *Energy Storage Mater.* *20*, 55–70.
35. Liu, J., Krishna, K.S., Kumara, C., Chattopadhyay, S., Shibata, T., Dass, A., and Kumar, C.S.S.R. (2016). Understanding Au₉₈Ag₄₄(SR)₆₀ nanoclusters through investigation of their electronic and local structure by X-ray absorption fine structure. *RSC Advances* *6*, 25368–25374.
36. Zhou, W.D., Wang, C.M., Zhang, Q.L., Abruna, H.D., He, Y., Wang, J.W., Mao, S.X., and Xiao, X.C. (2015). Tailoring Pore Size of Nitrogen-Doped Hollow Carbon Nanospheres for Confining Sulfur in Lithium-Sulfur Batteries. *Adv. Energy Mater.* *5*, 8.
37. Xu, Z.L., Kim, S.J., Chang, D., Park, K.Y., Dae, K.S., Dao, K.P., Yuk, J.M., and Kang, K. (2019). Visualization of regulated nucleation and growth of lithium sulfides for high energy lithium sulfur batteries. *Energy Environ. Sci.* *12*, 3144–3155.
38. Zhao, M., Peng, H.J., Li, B.Q., Chen, X., Xie, J., Liu, X., Zhang, Q., and Huang, J.Q. (2020). Electrochemical Phase Evolution of Metal-Based Pre-Catalysts for High-Rate Polysulfide Conversion. *Angew. Chem. Int. Ed. Engl.* *59*, 9011–9017.
39. Yan, Z., Liang, Y., Xiao, J., Lai, W., Wang, W., Xia, Q., Wang, Y., Gu, Q., Lu, H., Chou, S.L., et al. (2020). A High-Kinetics Sulfur Cathode with a Highly Efficient Mechanism for Superior Room-Temperature Na-S Batteries. *Adv. Mater.* *32*, e1906700.
40. Perdew, J.P., Burke, K., and Ernzerhof, M. (1996). Generalized gradient approximation made simple. *Phys. Rev. Lett.* *77*, 3865–3868.
41. Kresse, G., and Furthmüller, J. (1996). Effect of Er doping on the electronic structure optical properties of ZnO. *Phys. Rev. B Condens. Matter Mater. Phys.* *54*, 11169.